

Fig. 2. Normalised profiles of the modulus of the longitudinal mean flow velocity component (a) and rms values of longitudinal (b) and lateral velocity (c) fluctuations inside and above an urban street canyon. The wind tunnel measurement data are given by stars for the 120cm-long canyon and by diamonds for the 60cm-long canyon; the urban data from Rotach [14] are presented by filled circles; and the data from "smooth-rough" and "rough-rough" cases of Louka [15] are shown by filled and open triangles, respectively.

p11: Figure 2 in Kastner-Klein et al. (2001)

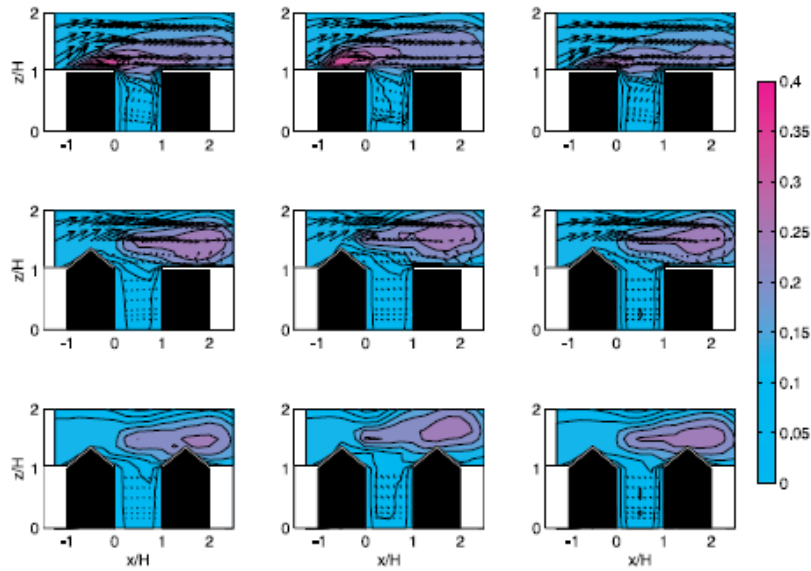


Fig. 3. Velocity in the central vertical plane of isolated street canyons with $L/H = 15$ (left plots), 10 (middle plots) and 5 (right plots) for three different roof configurations. The mean velocity field is shown by vectors, the colors refer to σ_u/u_0

p11: Figure 3 in Kastner-Klein et al. (2004a)

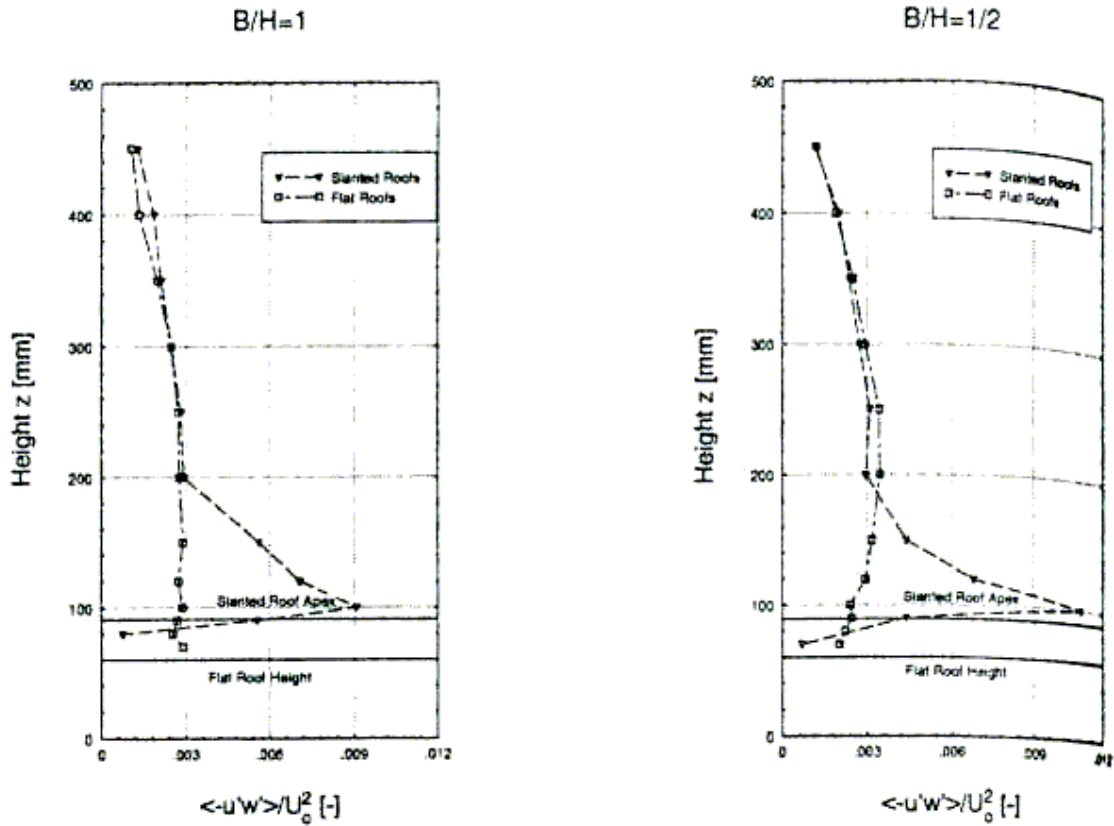


Figure 5. Vertical distribution of the Reynolds stress above urban fetches of flat and slanted roofs with street canyon aspect ratios $B/H = 1$ and $B/H = 1/2$.

p11: Figure 5 in Rafailidis (1997)

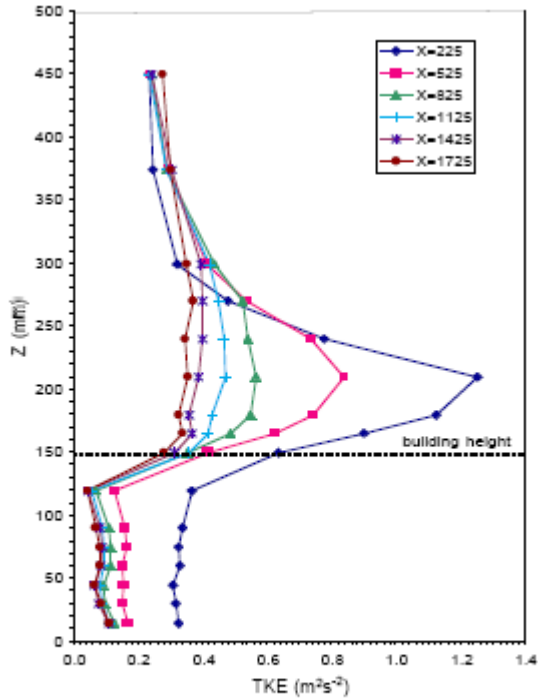


Figure 5. Turbulent kinetic energy profiles measured at the center of each of the canyons in the 2-d building array. Downwind position x in mm.

p12: Figure 5 in Brown et al. (2000)

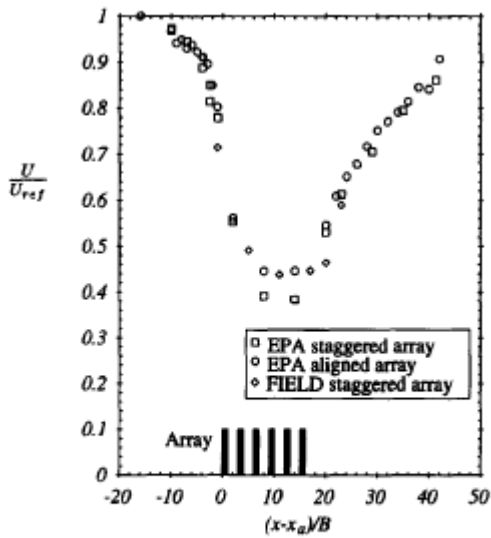


Fig. 5. Spatial (y -direction) and temporal average of the u -component of mean velocity measured at $z = H/2$, with the staggered and aligned obstacle arrays. U_{ref} is the magnitude of the velocity at $(x - x_a)/B = -16$.

p13: Figure 5 in Davidson et al. (1996)

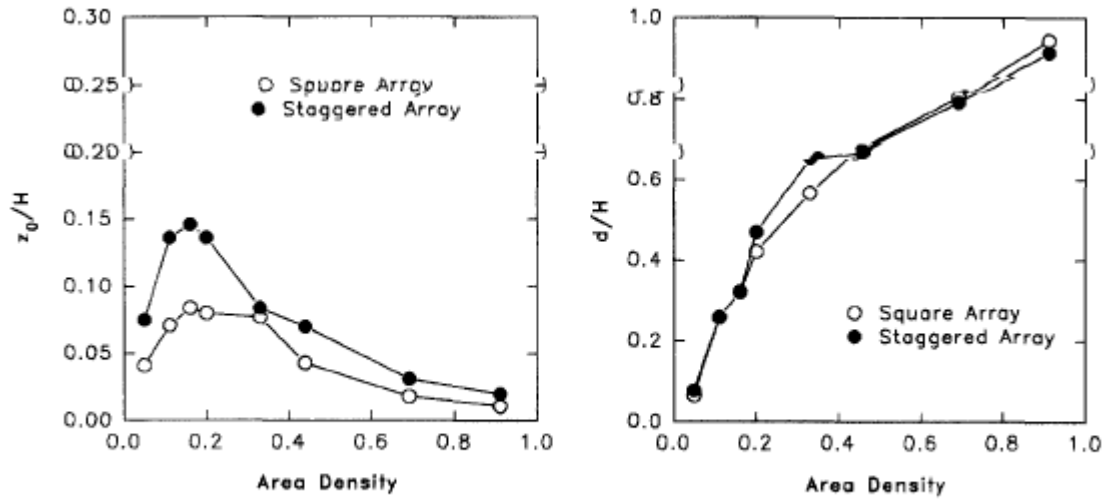


Fig. 2. Variation of z_0/H and d/H with area density for arrays of cubic obstacles in square and staggered geometries (data from Hall *et al.*, 1996).

p13: Figure 2 in MacDonald *et al* (1998a)

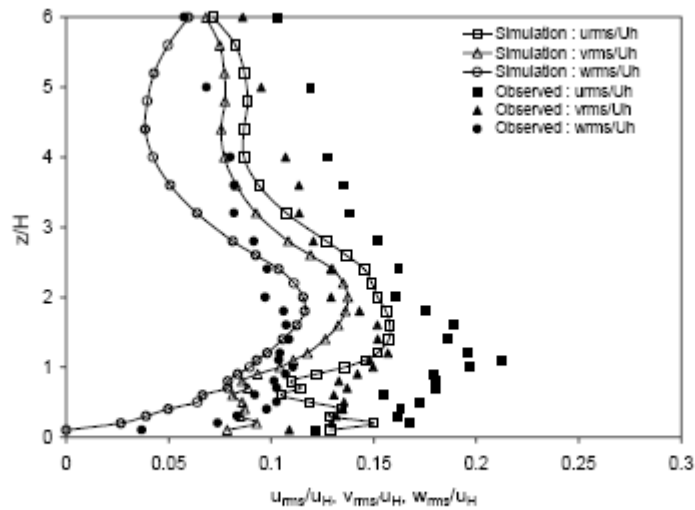


Fig. 4. Comparison of laterally averaged vertical profiles for turbulent intensities of the $f = 0.16$ square array configuration: numerical simulation (open symbols with line) behind the 7th row and observed (closed symbols) behind the 18th row.

p13: Figure 4 in Hanna *et al.* (2002)

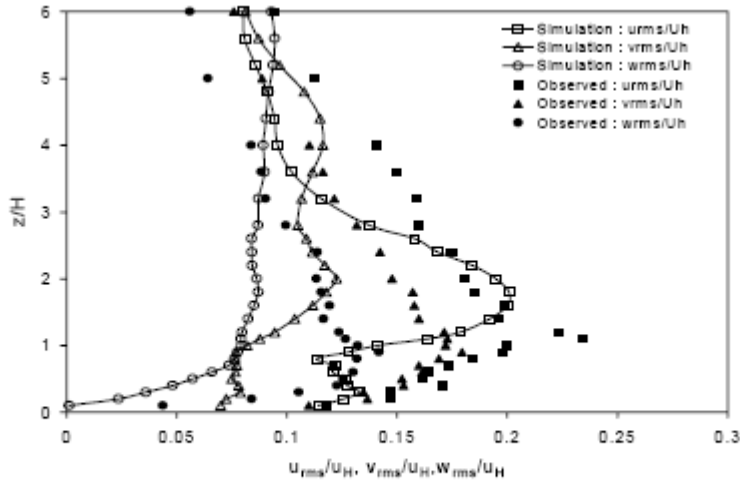


Fig. 6. Laterally averaged profiles for turbulent intensities of the $f = 0.16$ staggered array configuration: numerical simulation (open symbols with line) behind the 7th row and observed (closed symbols) behind the 18th row. The u , v , and w components are denoted by squares, triangles, and circles, respectively.

p13: Figure 6 from Hanna et al. (2002)

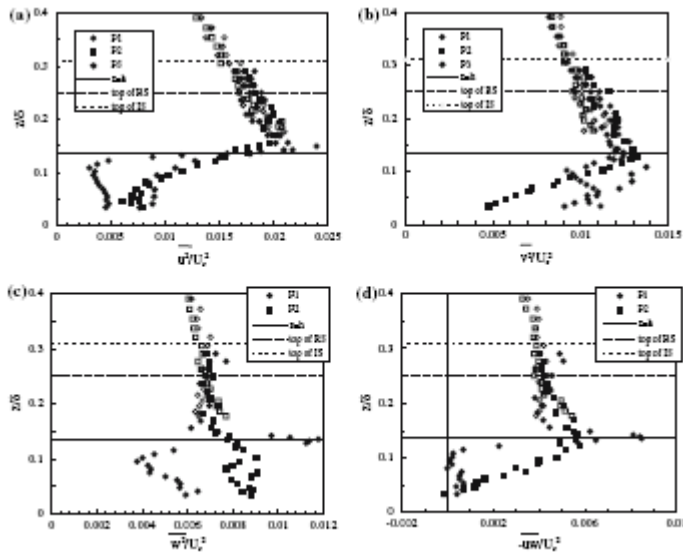


Figure 4. Reynolds stresses. Open symbols refer to HWA data.

p14: Figure 4 from Castro et al. (2006)

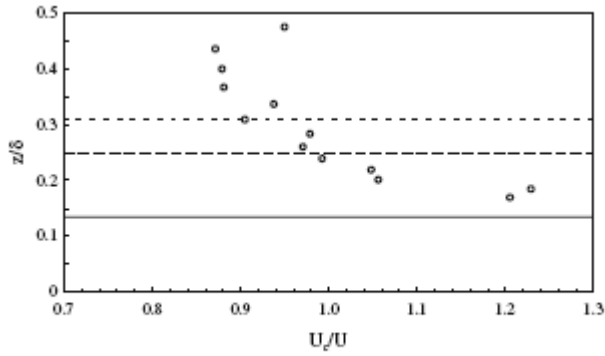


Figure 6. Convection velocity, U_c , at location P_2 . Solid, dashed and dotted lines mark the top of the canopy, roughness sublayer and inertial layer regions, respectively.

p14: Figure 6 from Castro et al. (2006)

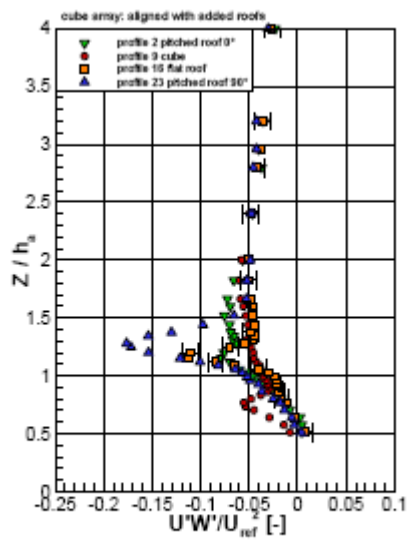


Figure 4: vertical turbulent flux profiles measured behind cubes with varying roof shape within and above the aligned array with roofs (configuration 2).

p15: Figure 4 in Schultz et al (2007)

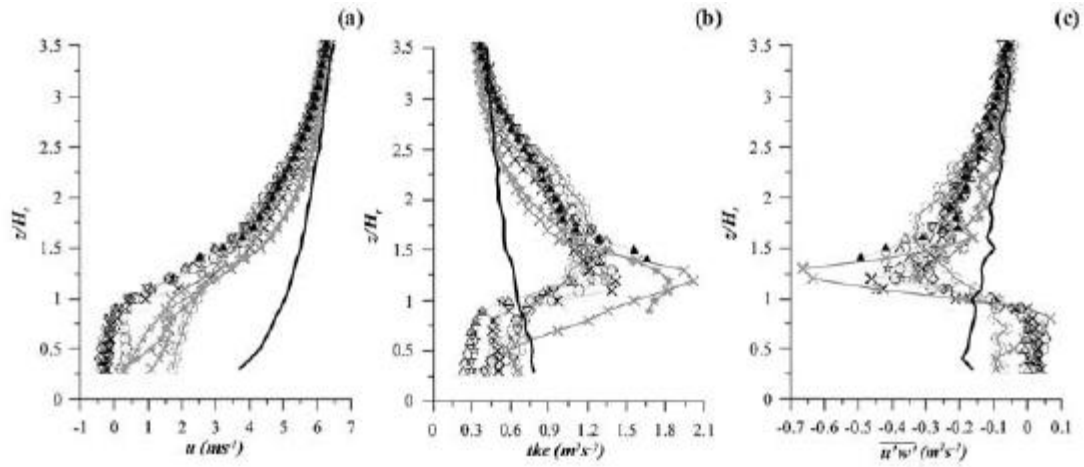


Figure 5. Measured profiles of (a) the mean u component, (b) turbulence kinetic energy and (c) turbulent shear stress of the Nantes wind-tunnel study (symbols according to Table II).

p15: Figure 5 in Kastner-Klein and Rotach (2004b)

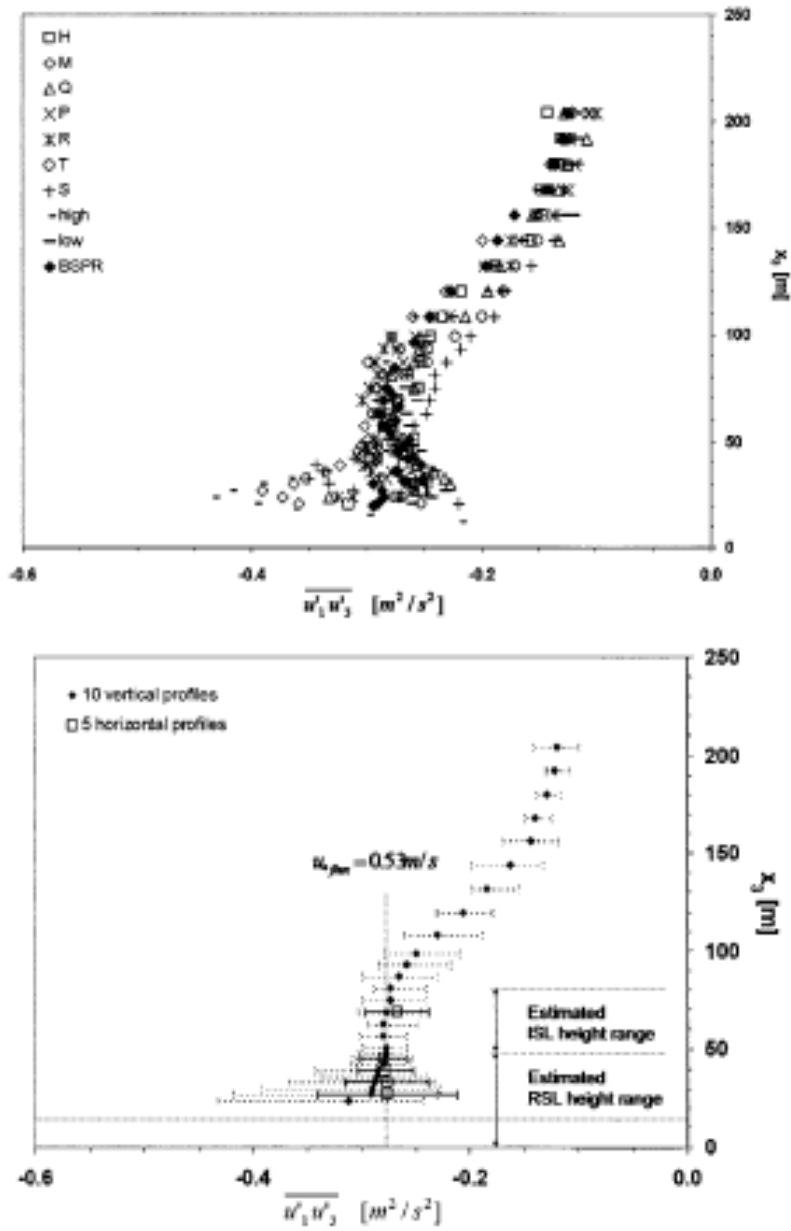


Figure 6.4: 10 vertical profiles of Reynolds fluxes (top) and horizontally averaged Reynolds fluxes (bottom). Dotted scatter bars refer to min-max range at each height level of the 10 vertical profiles, solid scatter bars give the standard deviation over each of the 5 horizontal profiles. See text for the estimated ISL height range.

p16: Figure 6.4 in Feddersen (2005)

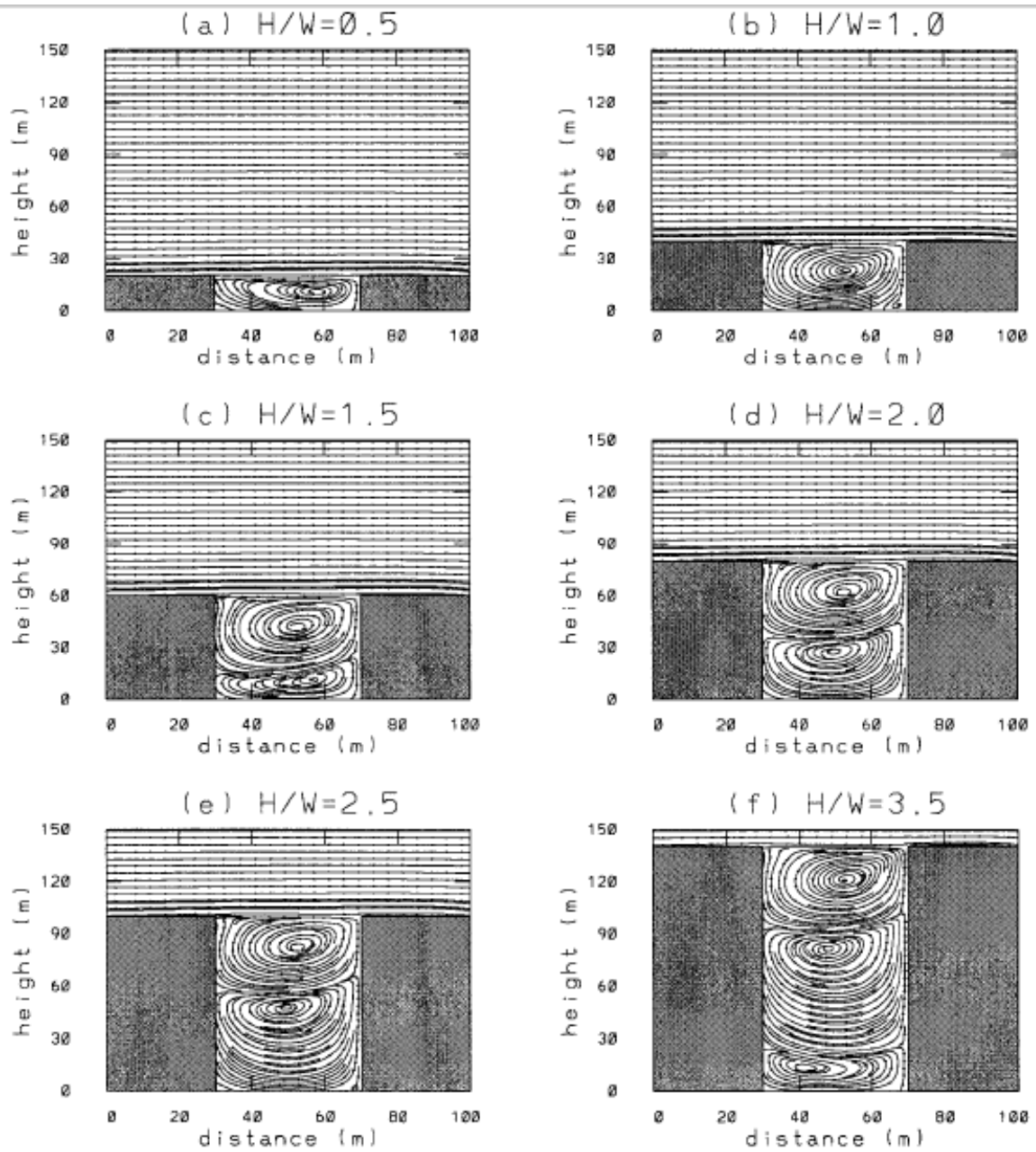


FIG. 3. Streamline fields at $t = 1$ h for street aspect ratios of (a) 0.5, (b) 1, (c) 1.5, (d) 2, (e) 2.5, and (f) 3.5.

p17: Figure 3 from Kim and Baik (1999)

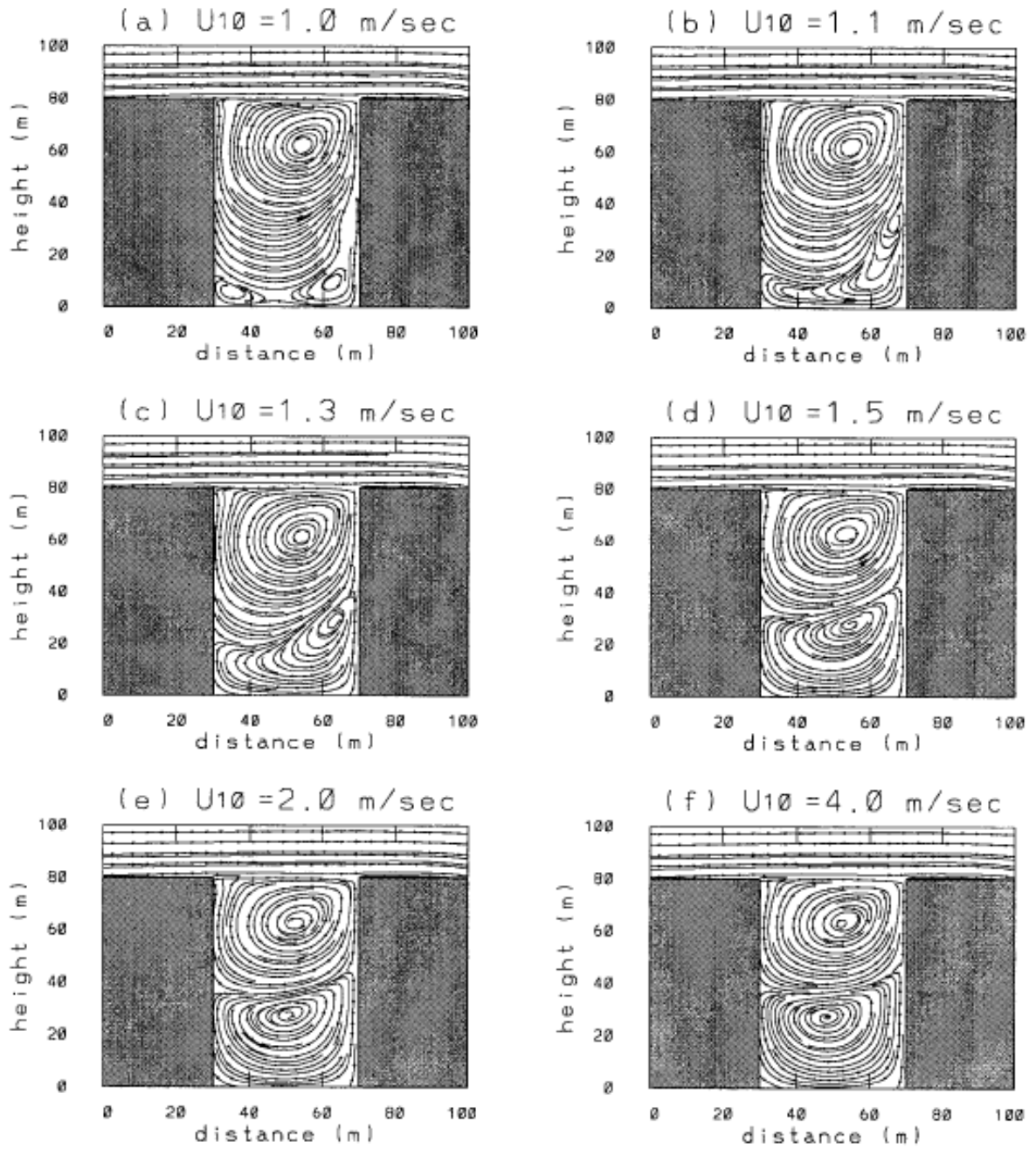


FIG. 9. Streamline fields at $t = 1$ h for an aspect ratio of 2 with different initial wind profiles. The initial wind speeds at the reference height ($z = 10$ m) are (a) 1, (b) 1.1, (c) 1.3, (d) 1.5, (e) 2, and (f) 4 m s^{-1} .

p17: Figure 9 from Kim and Baik (1999)

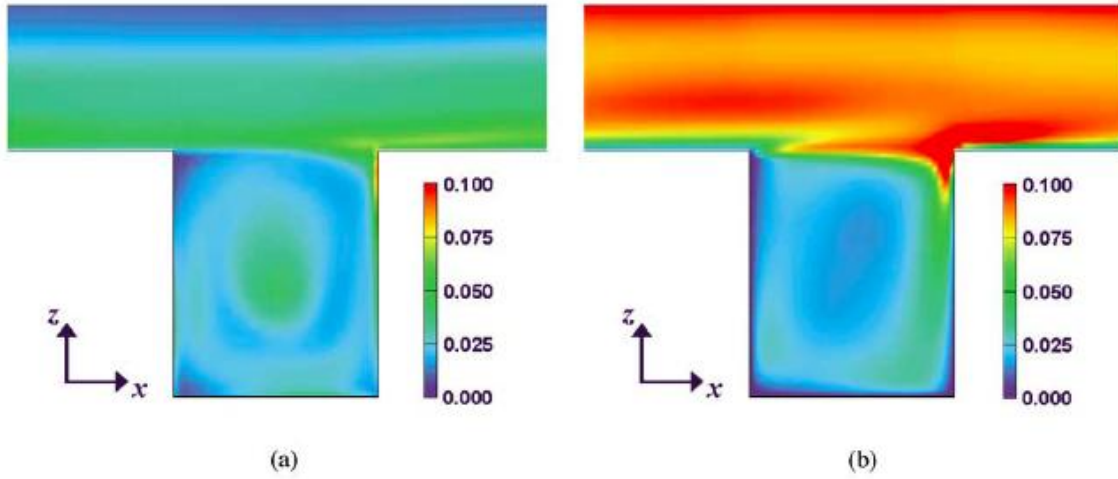


Fig. 11. Turbulence kinetic energy (k); normalised by u_{ref} : (a) LES; (b) $k-\varepsilon$ model.

p19: Figure 11 from Walton and Cheng (2002)

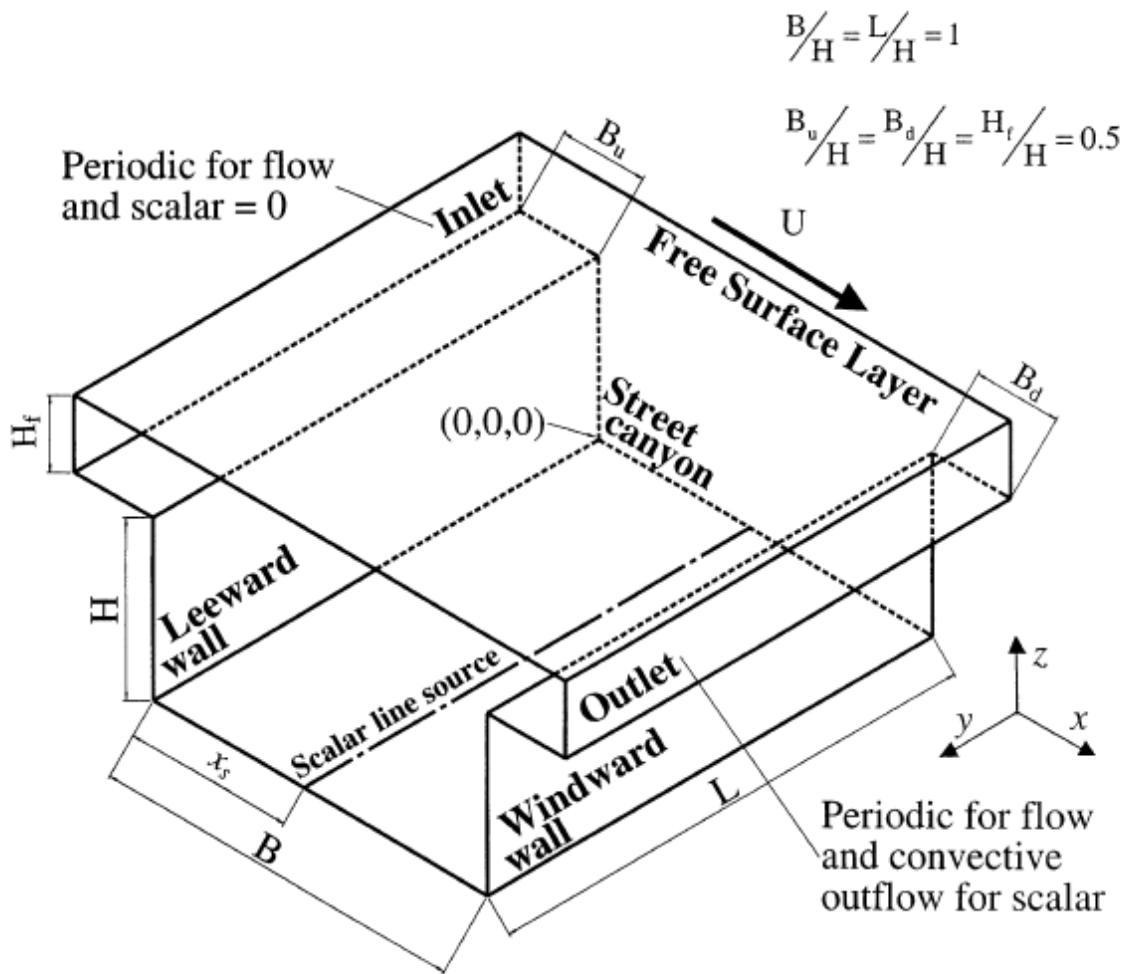


FIG. 4. Schematic diagram of the computational domain and boundary conditions for the flow and scalar transport in an idealized street canyon.

p19: Figure 4 from Liu & Barth (2002)



FIGURE 13. Iso-surfaces of ω_x near the smooth wall. Dark grey, +25.0%; light grey, -25.0% of $|\omega_x|_{Smax}$, respectively, or ± 0.37 wall units, normalized by $u_{\tau_s}^2/\nu$.



FIGURE 14. Iso-surfaces of ω_x near the rough wall. Dark grey, +5.0%; light grey, -5.0% of $|\omega_x|_{Rmax}$, respectively, or ± 0.19 wall units, normalized by $u_{\tau_R}^2/\nu$.

p21: Figures 13 & 14 from Ikeda & Durbin (2007)

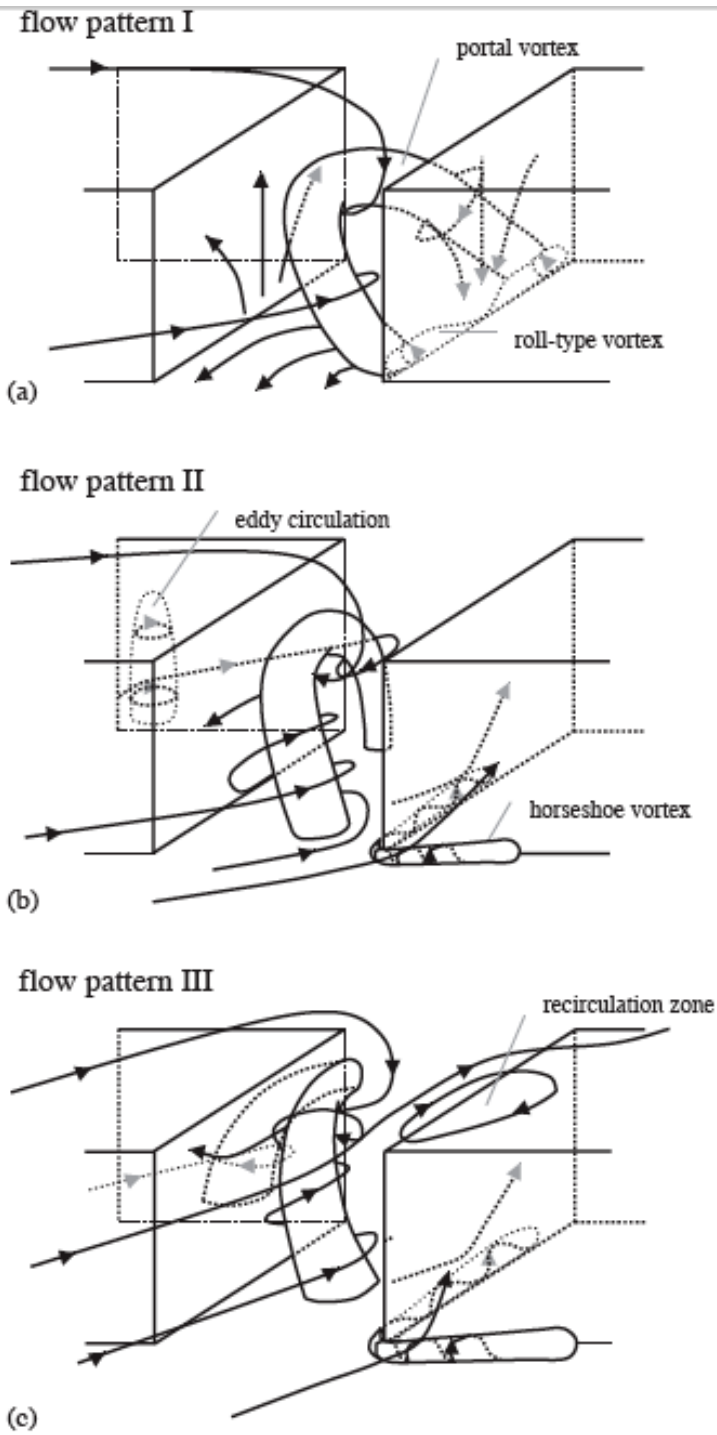


Fig. 4. The schematic of the mean flow circulation according to different ambient wind directions. The dimensions of the portal vortex depicted here are reduced for the clarity of figure.

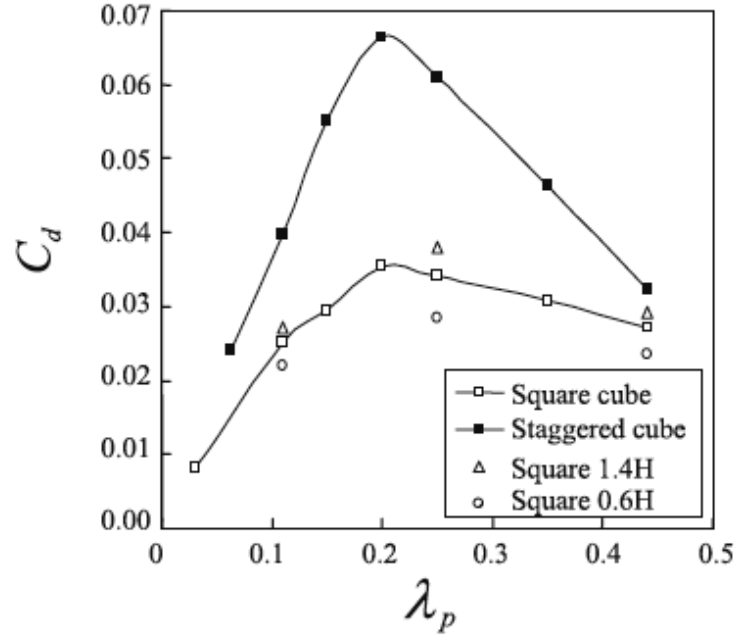


Figure 3. Temporally and horizontally averaged drag coefficients (at the peak Reynolds stress) for uniform-building arrays for various building area densities λ_p . The white and black squares represent the square- (run P03–P44 in Table I) and staggered-cube arrays (run S06–S44), respectively. The triangles and circles are from square arrays of the taller ($h = 1.4H$) and shorter ($h = 0.6H$) buildings, respectively.

p23: Figure 3 from Kanda (2006a)

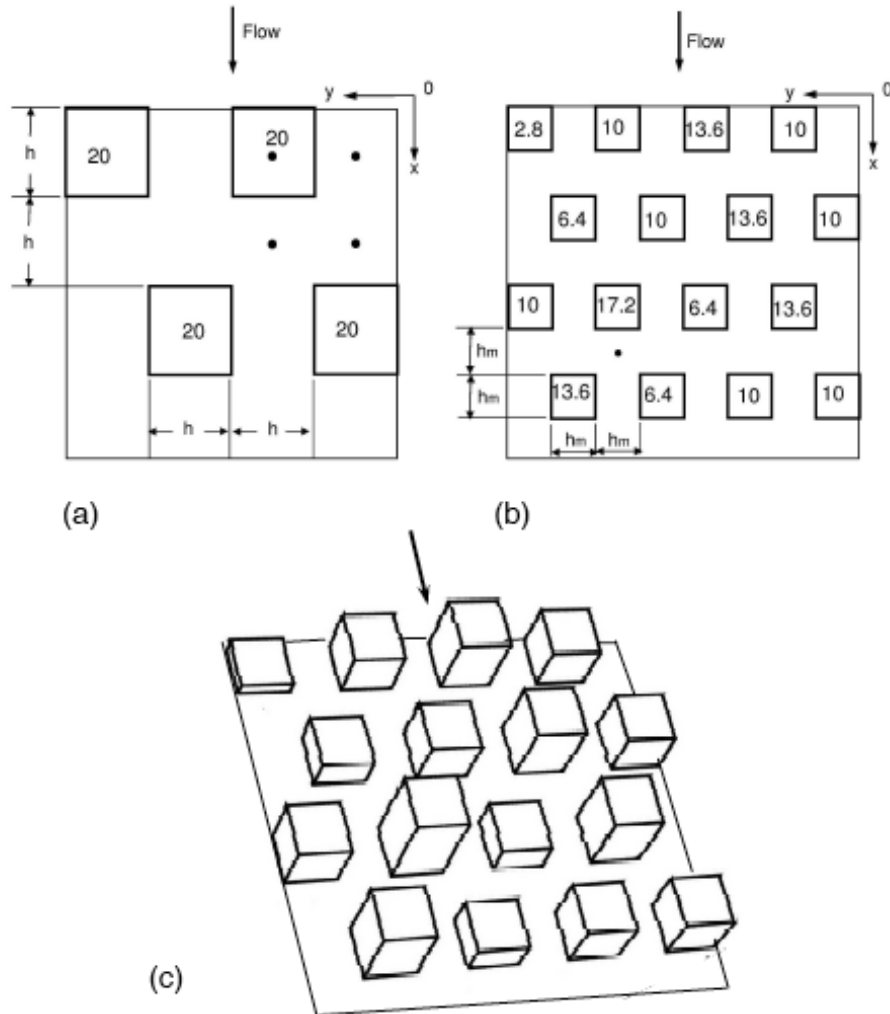


Figure 1. (a): schematic plan view of the domain for staggered cube arrays (case designated C20S); (b): schematic plan view of one unit of the domain for staggered random arrays, which consists of 2(streamwise) \times 2(lateral) units (designated RM10S). Dimensions in mm, with element heights indicated; (c): perspective view of one repeating unit of RM10S.

p24: Figure 1 from Xie & Castro (2006)

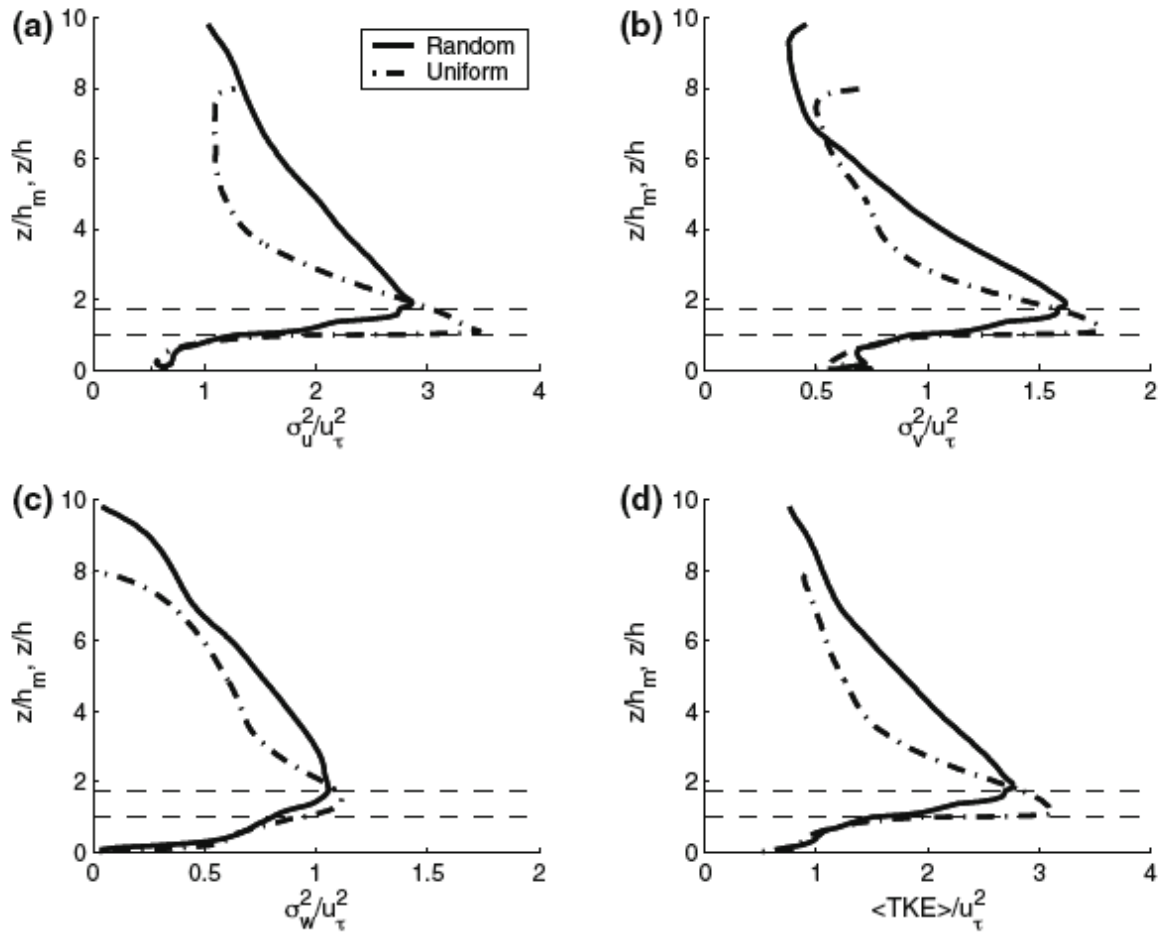


Fig. 12 Profiles of spatially-averaged streamwise, spanwise and vertical turbulent stresses and TKE

p24: Figure 12 from Xie et al (2008)

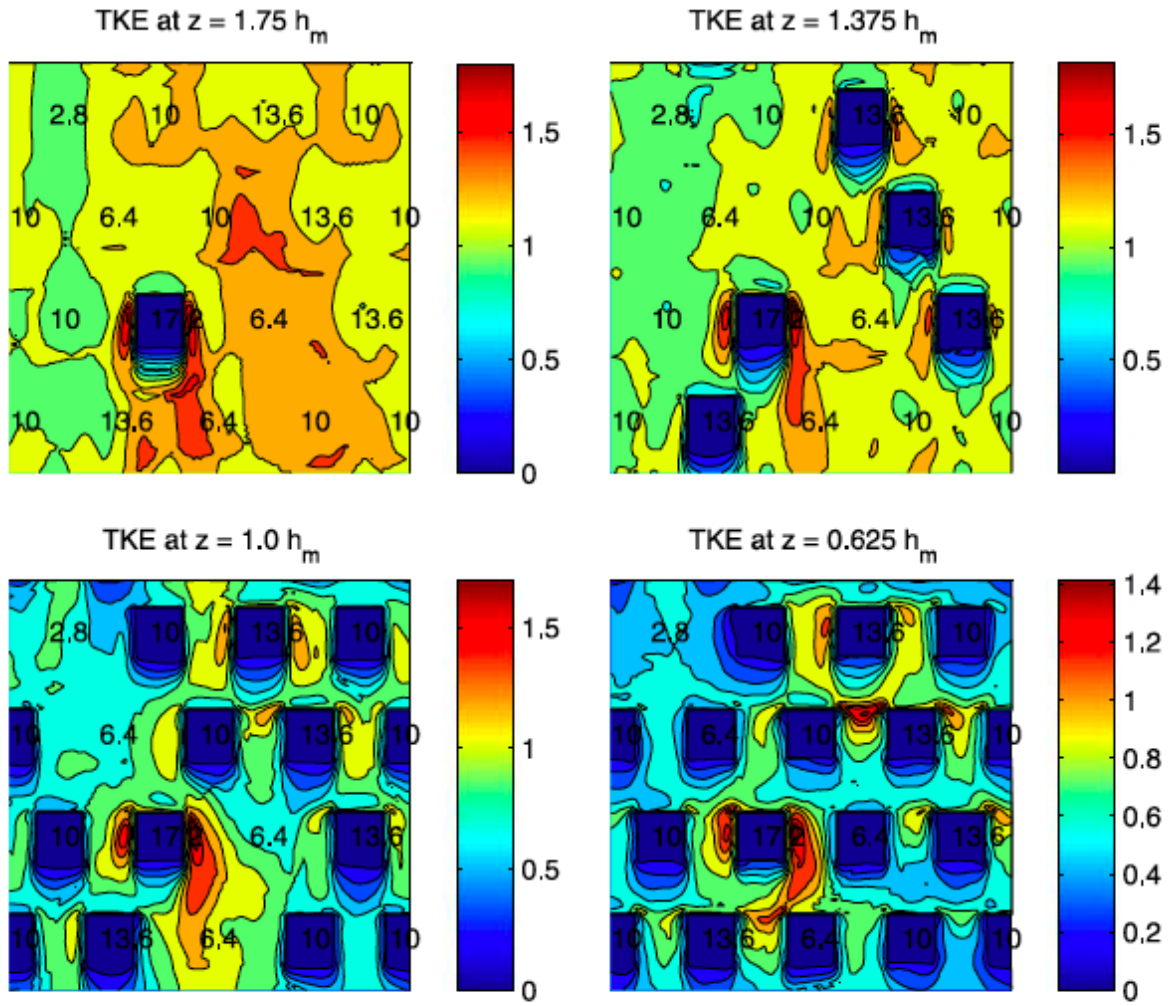


Fig. 9 TKE contours at $z/h_m = 0.625, 1.0, 1.375$ and 1.75 in a repeating unit. Flow is from top to bottom

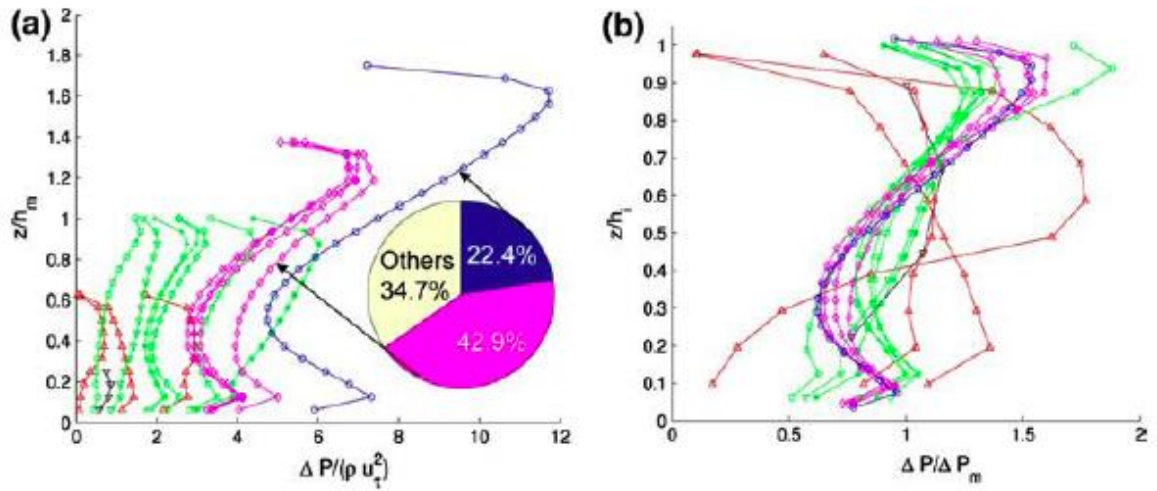


Fig. 10 Normalised profiles of the drag force on each of the 16 obstacles in a repeating unit of the random array. (a) the laterally integrated pressure difference between the front and back faces of the cube, normalised by ρu_τ^2 . (b) pressure difference normalised by the mean pressure difference on each block, with z normalised by the individual block height

p24: Figures 9 & 10 from Xie et al (2008)

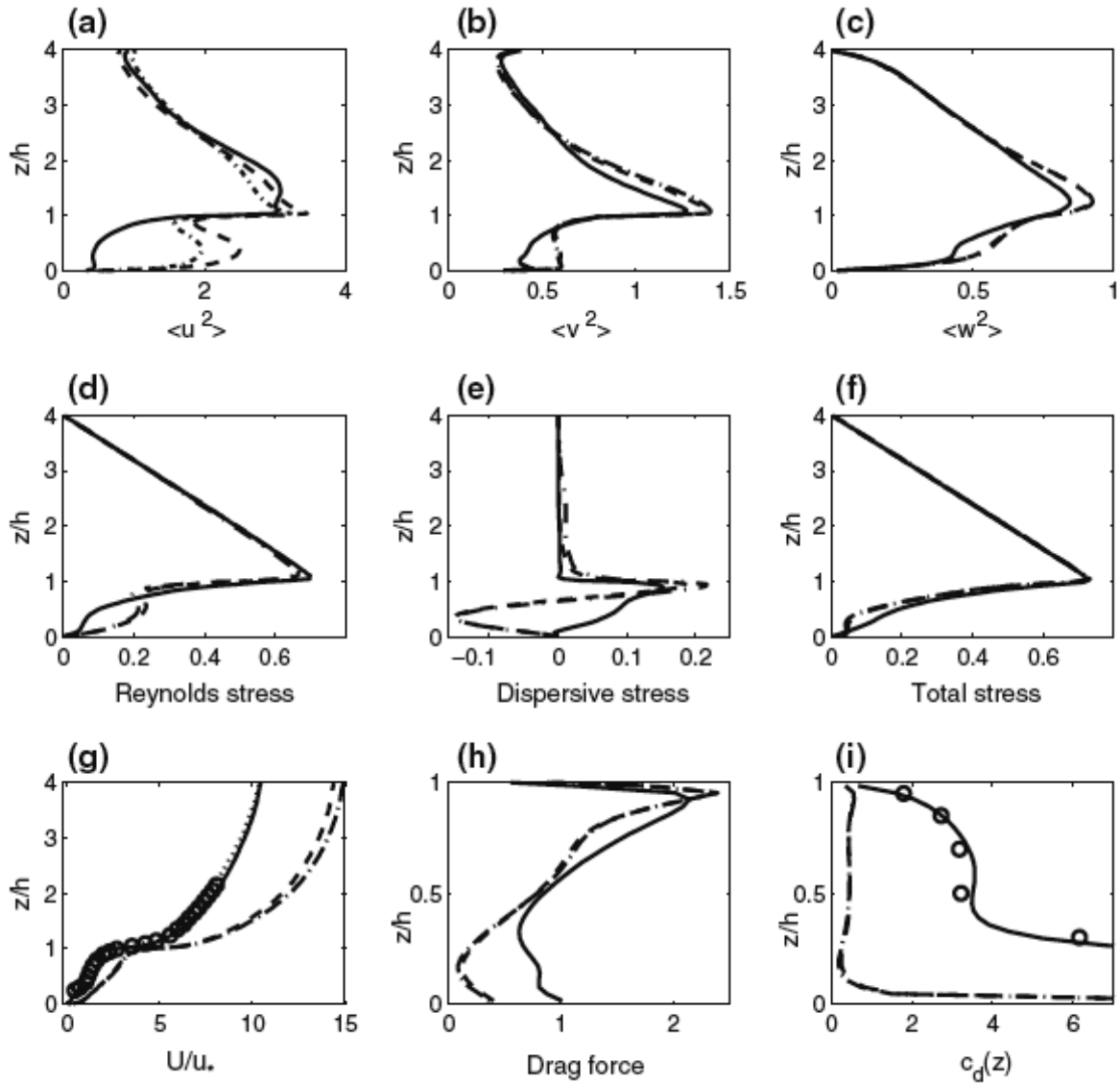


Fig. 20 Dependence of computed statistics on layout of roughness array. Solid lines: staggered array. Dashed lines: aligned array. Dot-dashed line: square array. Dotted line: spatial average of mean streamwise velocity in staggered array using only four sampling points per repeating unit. Circles: wind tunnel data from Cheng and Castro (2002) for staggered array. (a) $\langle \overline{u^2} \rangle$ (b) $\langle \overline{v^2} \rangle$ (c) $\langle \overline{w^2} \rangle$ (d) shear stress $\langle \overline{u'w'} \rangle$ (e) dispersive stress $\langle \overline{\tilde{u}\tilde{w}} \rangle$ (f) total stress $\langle \overline{u'w'} \rangle + \langle \overline{\tilde{u}\tilde{w}} \rangle + \nu \partial \langle \overline{u} \rangle / \partial z$ (g) horizontally-averaged mean streamwise velocity $U \equiv \langle \overline{u} \rangle$ (h) drag force $F_d(z)$ (i) sectional drag coefficient $c_d(z)$

p25: Figure 20 from Coceal et al (2006)

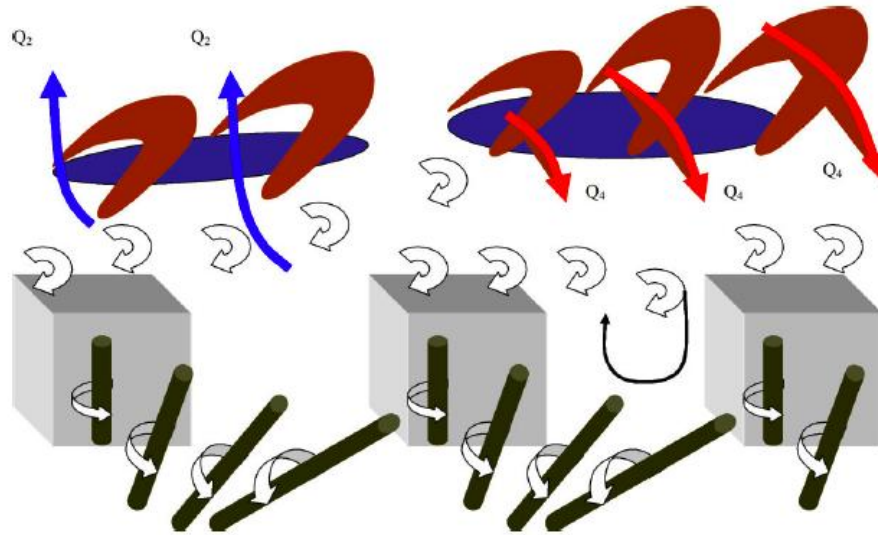


Figure 10. Conceptual cartoon summarising the unsteady flow dynamics above and within groups of buildings. Above the buildings momentum transport is dominated by large hairpin-shaped eddies (brown) with associated low momentum regions (blue). Q_2 denotes an ejection event between the hairpin vortex legs and Q_4 denotes a sweep event on the sides. Within the building canopy eddies shed off the vertical edges of the buildings are rotated by the mean shear. Strong canopy-top shear layers intermittently penetrate into the canopy, impacting upon buildings downstream and driving a recirculation in front of the buildings. This figure is available in colour online at www.interscience.wiley.com/ijoc

p25: Figure 10 from Coceal et al (2007c)

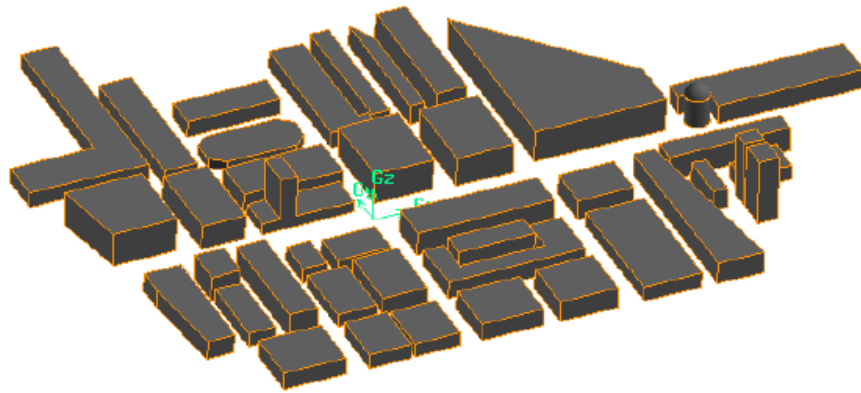


Figure 3. The 1:200 scale model of the Marylebone area topography that was represented in the CFD simulation. The computational domain extends however to a further distance upwind and downwind from the outer most obstacles as flat terrain described in section 3.

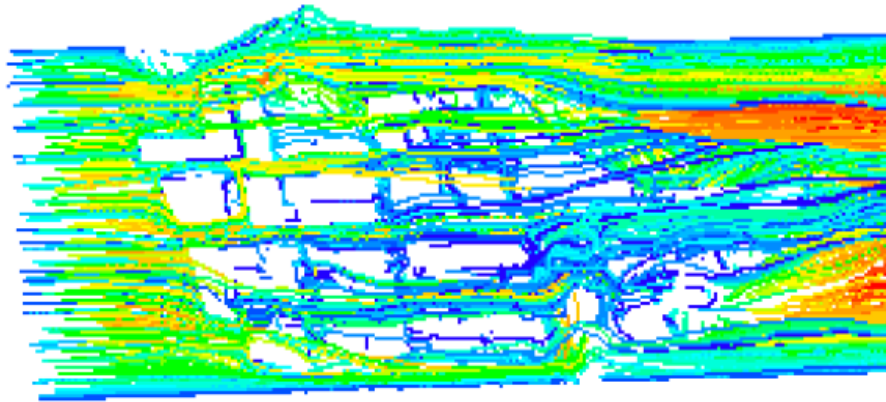
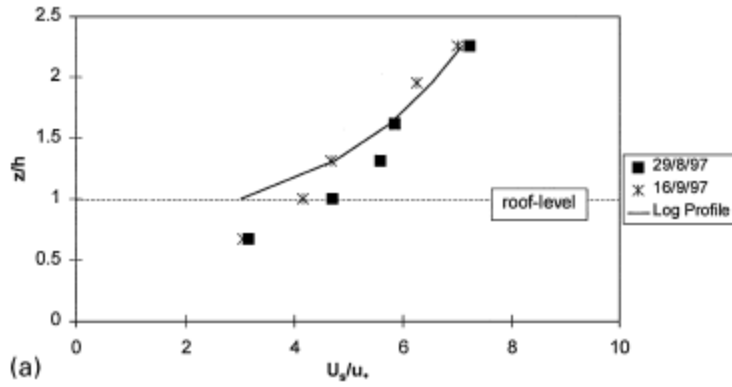
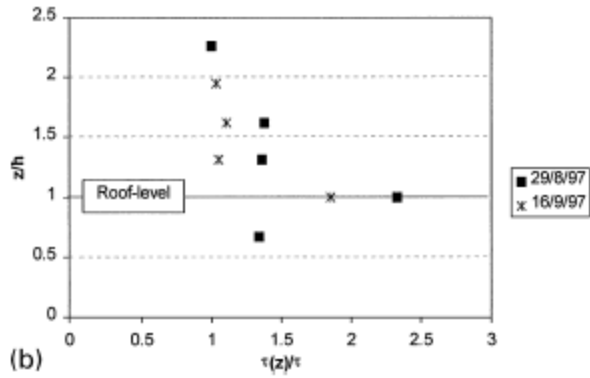


Figure 4: Path lines of mass-less tracer particles to visualize the 3-D flow.

p26: Figures 3 & 4 from Neophytou & Britter (2005)



(a)



(b)

Fig. 3. (a) Vertical profile of U_s/u_* . The solid line represents the logarithmic profile fitted to the three highest levels. (b) Vertical profile of the Reynolds stress normalised with the value at the highest level.

p28: Figure 3 in Louka et al. (2000)

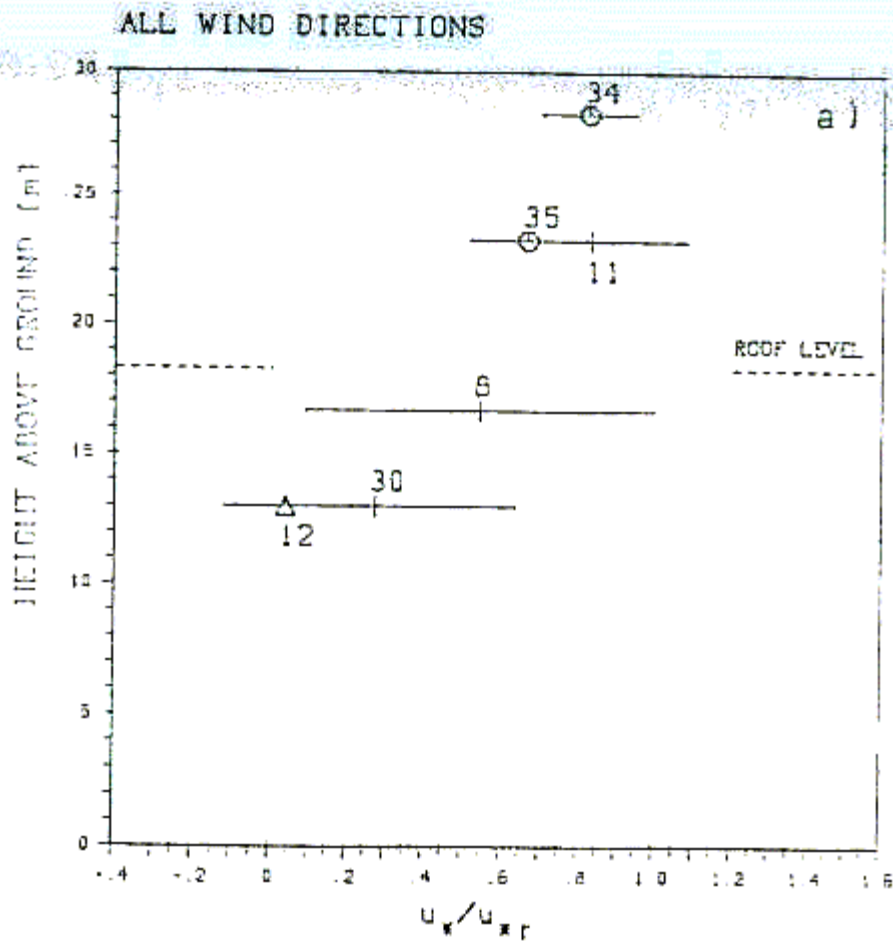


Fig. 4(a).

p29: Figure 4a in Rotach 1993a

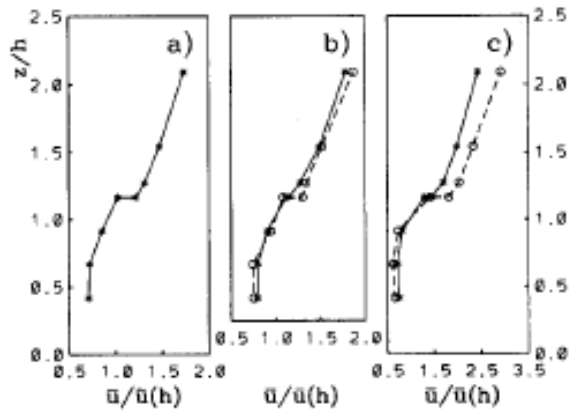


Fig. 2. Average profiles of the magnitude of wind speed, scaled by its value at $z = h$: (a) averaged over all available data; (b) approaching flow normal to the canyon from SW (full line and stars) and parallel to the canyon (dashed line and circles); (c) approaching flow normal to the canyon from NE (full line and stars) and the same but only runs with wind speed larger than 3 m s^{-1} at position 21R (dashed line and circles).

p29: Figure 2 in Rotach 1995

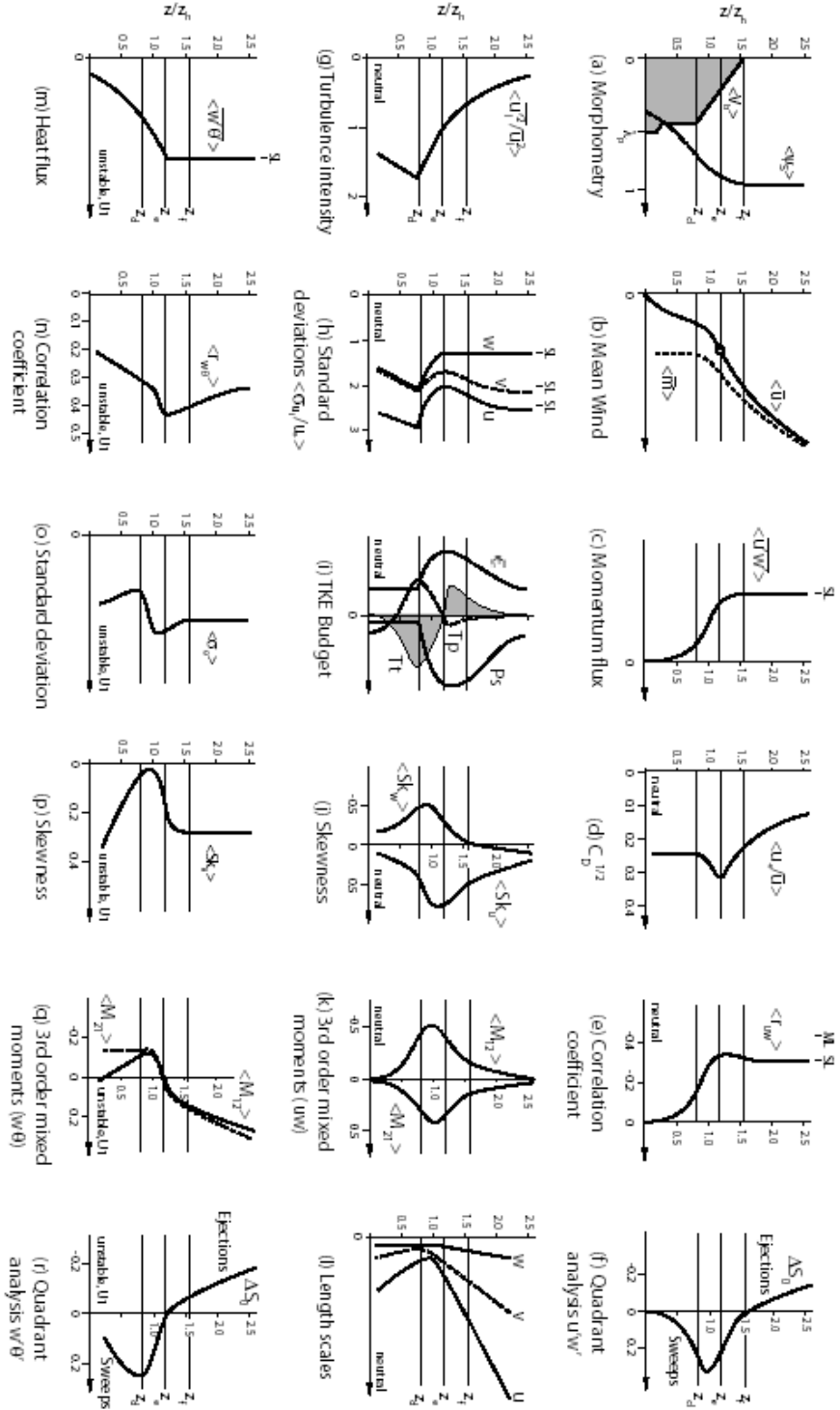
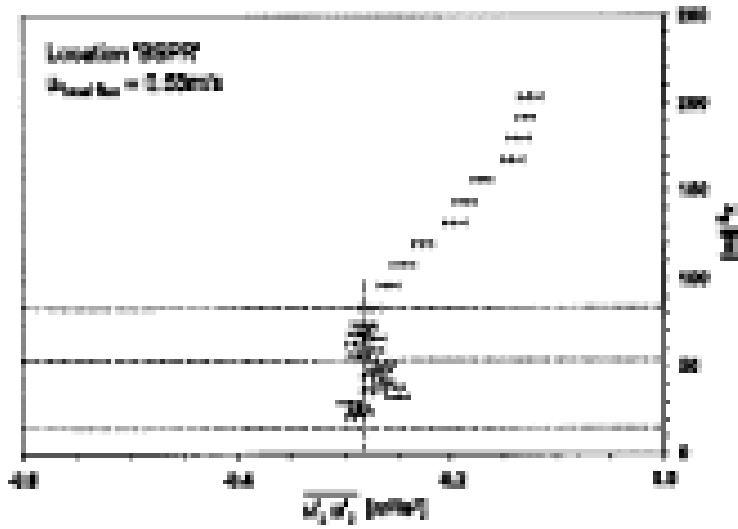


Figure 5.1: Concept of generalized and horizontally averaged profiles through the roughness sublayer derived from the present study. The three reference heights are zeroplane displacement z_d , the effective building height (height of the wind profile inflection point) z_{e1} and the height of maximal Reynolds stress z_f . (a) Building volume density (V_b) in $m^3 m^{-3}$ in a given layer and sky view factor (ψ_s). (b) global longitudinal wind velocity (\bar{u}) and horizontal scalar wind speed (\bar{m}). (c) turbulent momentum flux ($\overline{u'w'}$). (d) square root of the neutral drag coefficient (\bar{u}_c/\bar{u}). (e) correlation coefficient of turbulent momentum flux (r_{uw}). (f) the quadrant measure $\Delta S_0^w(u'w')$ indicating if sweeps or ejections are dominant in the turbulent momentum flux. (g) local turbulence intensity expressed as the local ratio between turbulent TKE and MEK under neutral conditions (w_r^2/\bar{u}^2). (h) neutral limits of locally scaled standard deviations (σ_u/\bar{u}_c). (i) the relevant terms of the neutral TKE-budget (P_s : shear production, T_P : tubular transport, T_P : pressure transport, ϵ : dissipation rate). (j) skewness of horizontal (S_{k_u}) and vertical wind component (S_{k_w}). (k) third order mixed moments of u and w (M_{12} : $\overline{u^2 w'}$, M_{21} : $\overline{u' w^2}$, M_{13} : $\overline{u' w \theta}$, M_{31} : $\overline{w \theta u'}$, M_{22} : $\overline{u' w^2}$, M_{32} : $\overline{w \theta w'}$, M_{23} : $\overline{u' w \theta}$, M_{33} : $\overline{w \theta w'}$). (l) Integral length scales derived from peak frequency of power spectra. (m) turbulent heat flux ($\overline{w'\theta}$). (n) correlation coefficient of turbulent heat flux ($r_{w\theta}$). (o) Standard deviation of temperature σ_θ . (p) skewness of temperature (S_{k_θ}). (q) third order mixed moments of w and θ (M_{12} : $\overline{w^2 \theta'}$, M_{21} : $\overline{w' \theta^2}$, M_{13} : $\overline{w' \theta w'}$, M_{31} : $\overline{w \theta w'}$, M_{22} : $\overline{w' \theta^2}$, M_{32} : $\overline{w \theta w'}$, M_{23} : $\overline{w' \theta w'}$, M_{33} : $\overline{w \theta w'}$). (r) the quadrant measure $\Delta S_0^{w/\theta}$ for turbulent heat flux. 'ML' and 'SL' denote surface layer and plane mixing layer limits, respectively.



p30: Figure D2 in Appendix D of Feddersen (2005). x-axis shows shear stress component $\overline{u'w'}$, z-axis shows height z (m). Horizontal lines indicate mean building height (bottom), RSL depth (middle) and ISL top (top). Vertical line indicates ISL mean shear stress value.

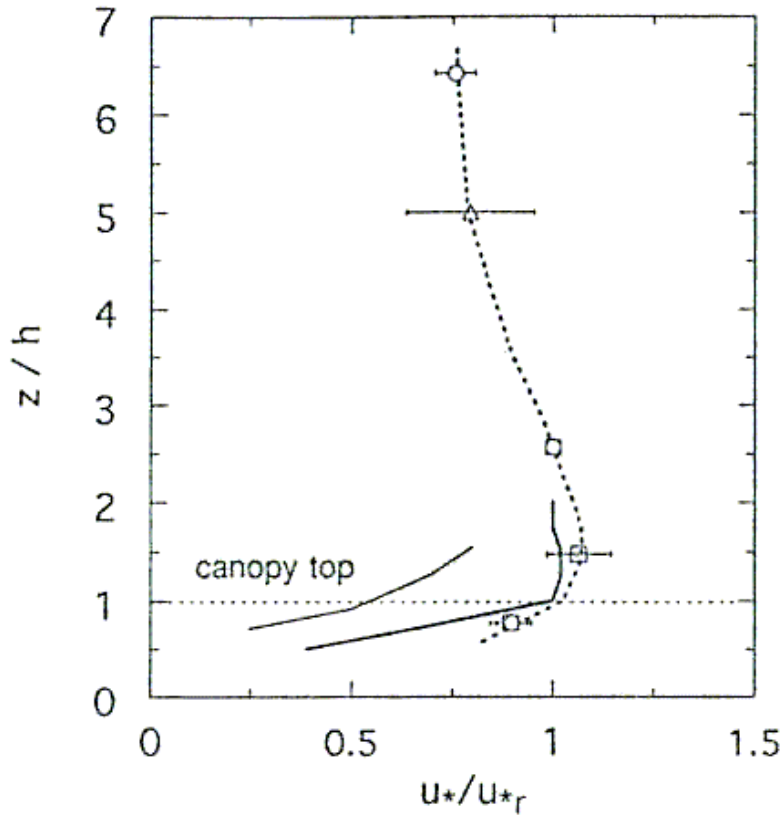


Fig. 4. The normalized Reynolds stress profiles. The dashed curve was drawn by eye. The details of the symbols and the line follow Figure 3(b)–(d).

p32: Figure 4 in Oikawa and Meng (1995)

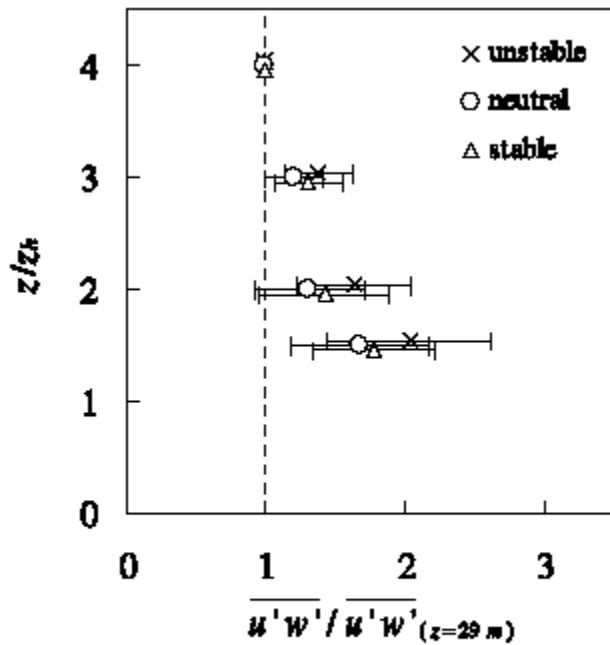


Fig. 3. Profiles of shear stress scaled to the stress measured at 29 m ($=4 \times z_h$). Error bars represent the run-to-run variability (standard deviation)

p32: Figure 3 in Moriwaki and Kanda (2006d)

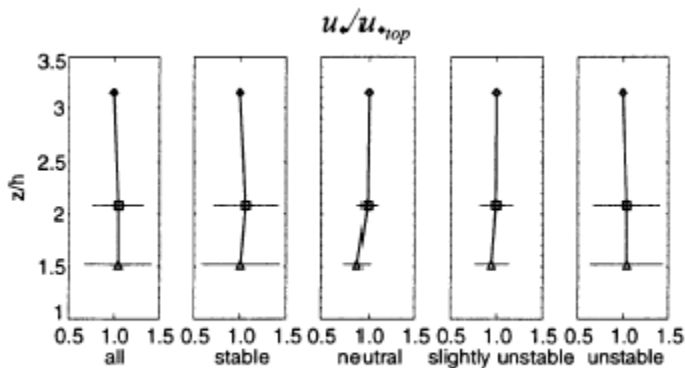


Fig. 4. Scaled profiles of friction velocity u^*

p34: Figure 4 from Feigenwinter et al. (1999)

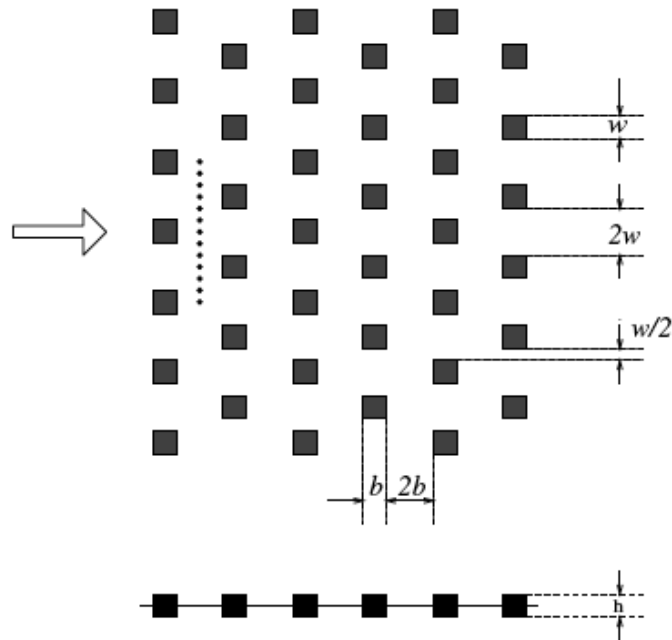


Figure 12. Array of obstacles used in the experiments of Davidson *et al.* (1995, 1996). A side view is shown below a plan view. Dots indicate the position of measurements.

p39: Figure 12 from Coceal & Belcher (2004)

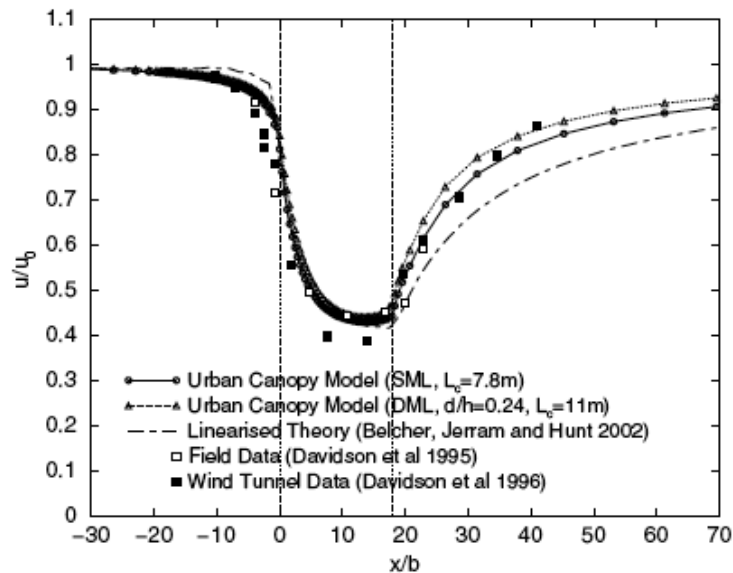


Figure 13. Deceleration of mean wind at half the roughness element height through canopy of roughness elements. Comparison of the urban canopy model with the measurements of Davidson *et al.* (1995, 1996). The canopy lies between $x/b = 0$ and 18; b is defined in Fig. 12.

p39: Figure 13 from Coceal & Belcher (2004)

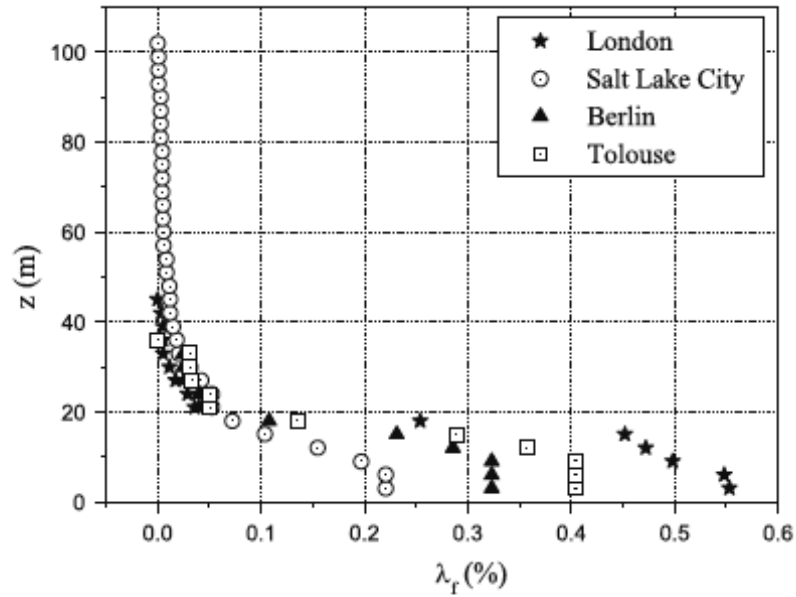


Fig. 6 Profile of $\lambda_f(z)$ for London, Toulouse, Berlin and Salt lake City calculated from DEM analysis

p39: Figure 6 from Di Sabatino et al. (2008)

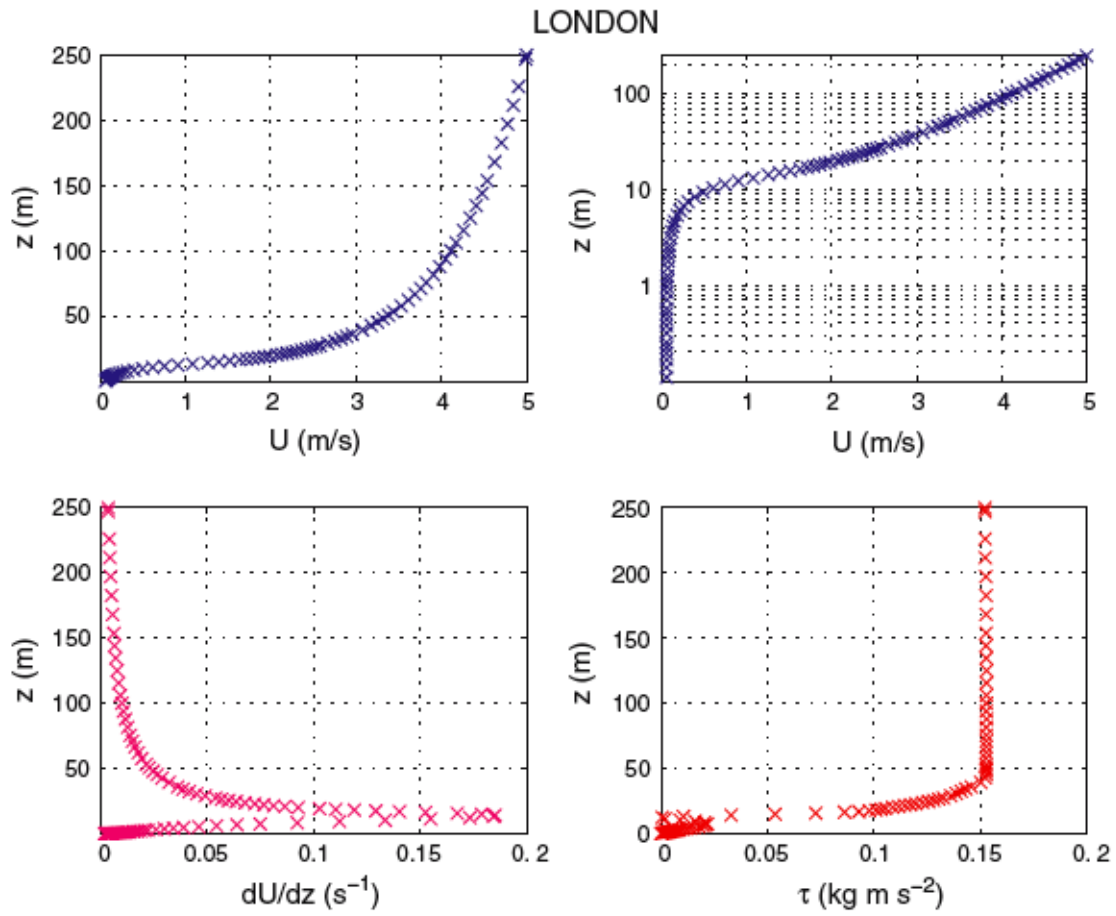


Fig. 7 Model results for London using λ_f variation with height. Mean velocity profiles (upper plots), mean velocity first derivative and shear stress profiles (lower plots)

p39: Figure 7 from Di Sabatino et al. (2008)

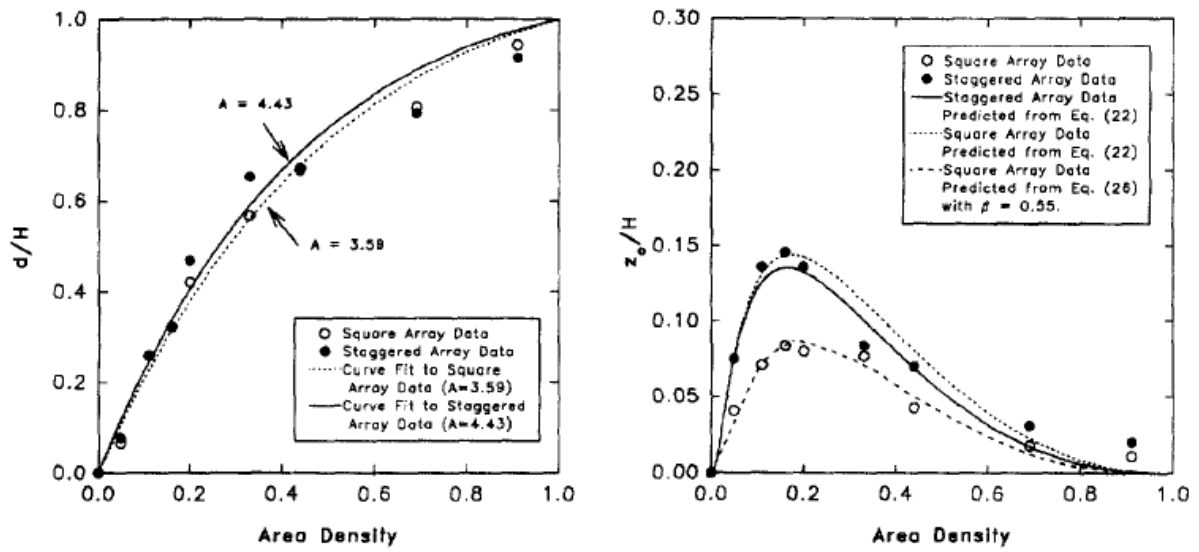


Fig. 4. Best fit models for the displacement height data and the resulting curves of the z_0/H variation compared to the experimental data for square and staggered arrays of cubes.

p40: Figure 4 from Macdonald et al. (1998)

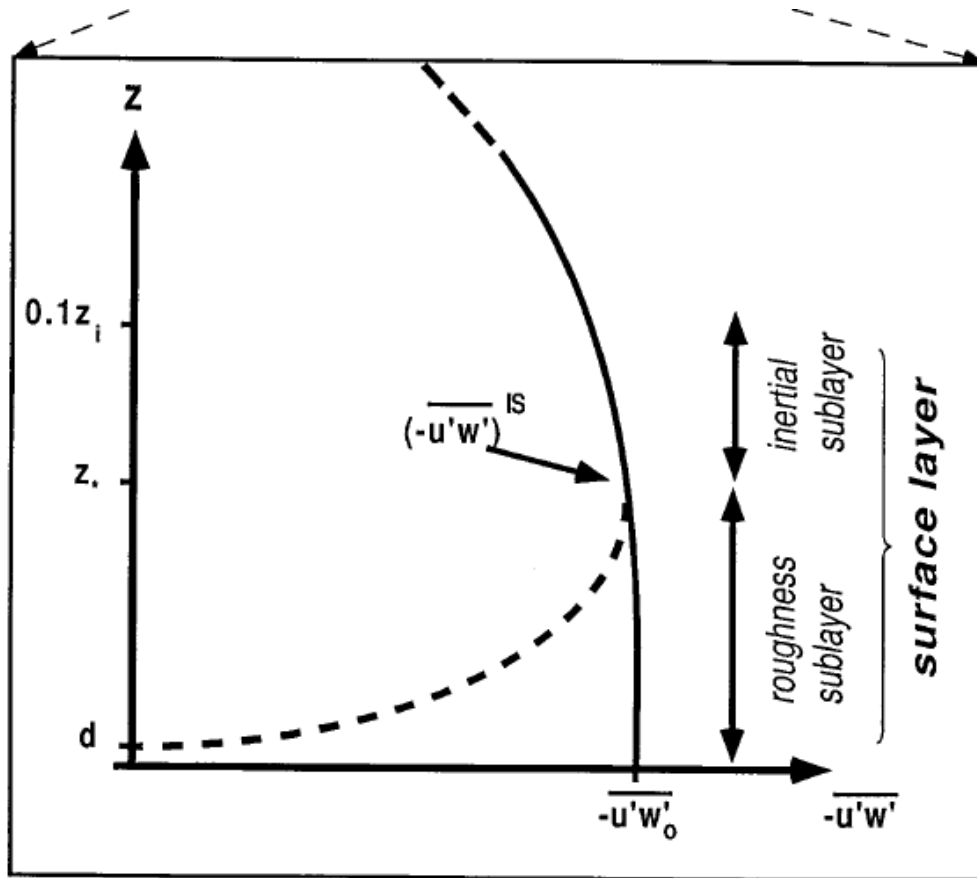


Figure 1. Conceptual sketch of Reynolds stress in the urban boundary layer. The solid line corresponds to a parameterisation according to de Haan and Rotach (1998), which slightly departs from the 'standard' linear profile (cf. the upper part of the figure) in that it assumes an approximately constant value when approaching the surface.

p40: Part of Figure 1 from Rotach (2001)

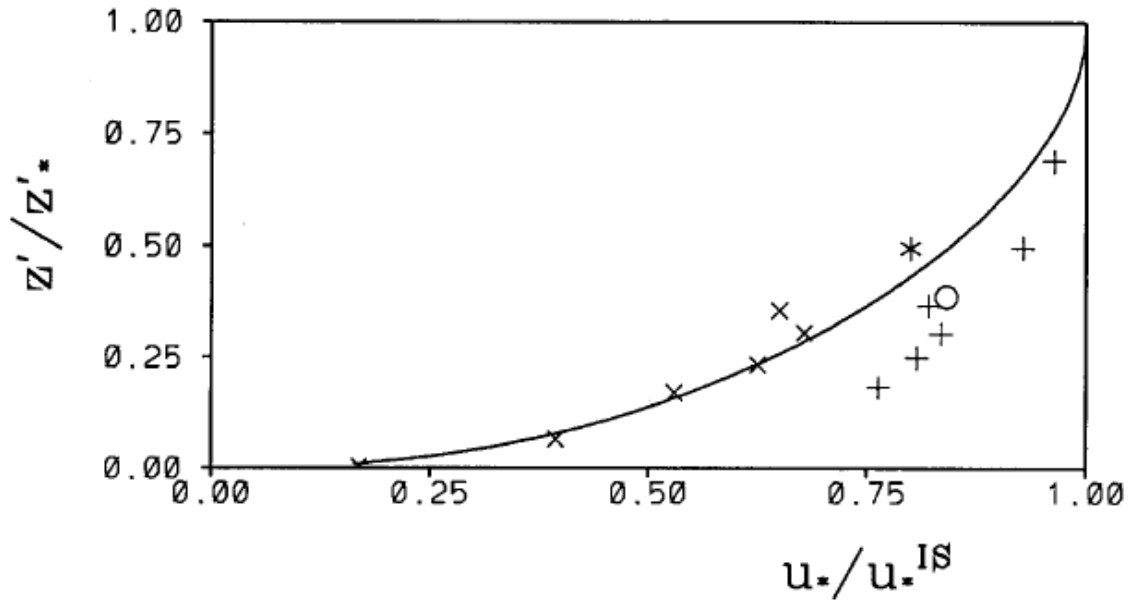


Figure 2. Parameterised profile of (local) friction velocity, u_* , as a function of non-dimensional height, Equation (1). The symbols refer to the full-scale data of Rotach (1993a), x ; Oikawa and Meng (1995), $*$ and Feigenwinter et al. (1998), o . Wind-tunnel data after Rafailidis (1997), $+$, are shown for comparison. The latter are not employed to fit the parameters in Equation (1) (only the 'flat roof' experiments with aspect ratio 1/2 shown).

p40: Figure 2 from Rotach (2001)

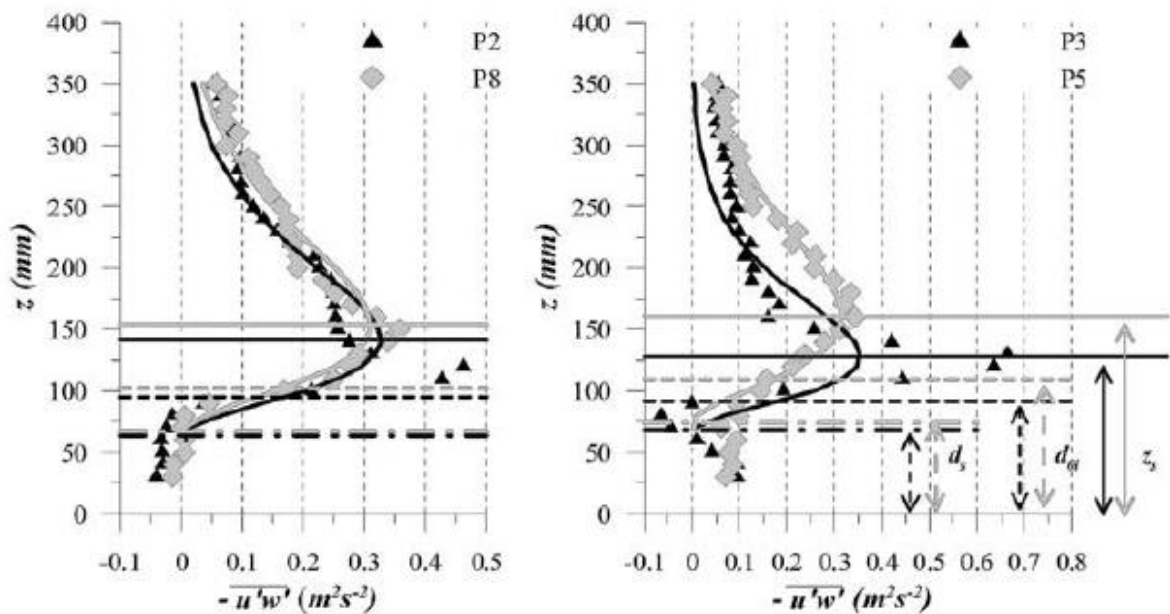


Figure 9. Illustration of the shear-stress approximation and corresponding length scales for four measured shear-stress profiles.

p41: Figure 9 from Kastner-Klein & Rotach (2004)

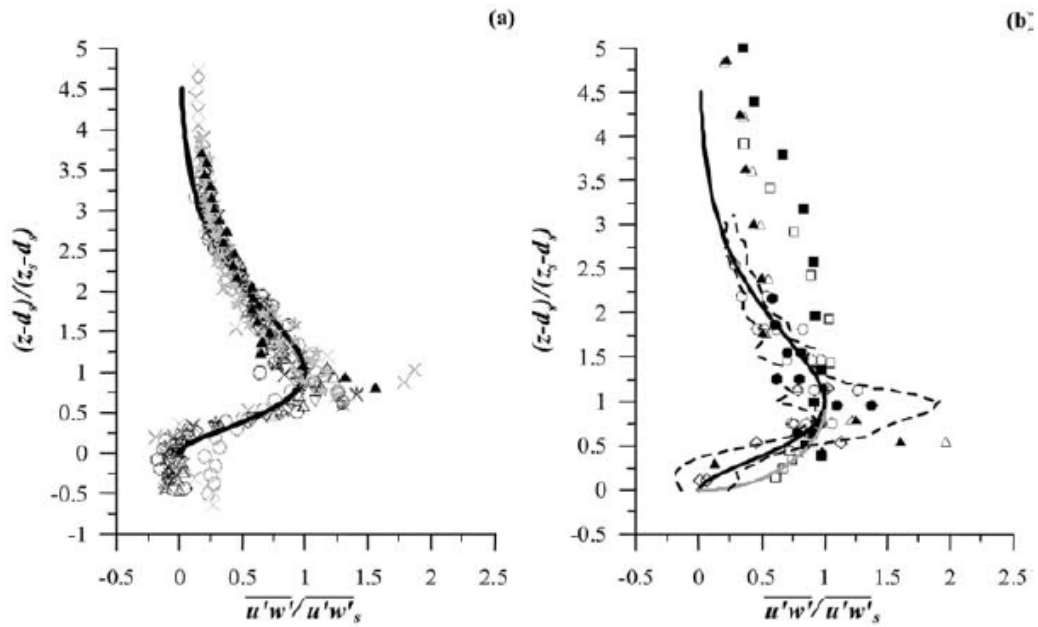


Figure 10. (a) Scaling of wind-tunnel shear stress profiles measured in the Nantes study (symbols according to Table II) and (b) comparison of proposed shear-stress parameterizations according to Equations (4) and (10) with full-scale and wind-tunnel data published in the literature (Rotach (1993a): \diamond ; Louka (1999), smooth-rough case: \circ , rough-rough case: \bullet ; Oikawa and Meng (1995): \star , Rafailidis (1997), aspect ratio $S/H = 1$ with flat roofs: \blacksquare , aspect ratio $S/H = 0.5$ with flat roofs: \square , aspect ratio $S/H = 1$ with slanted roofs: \blacktriangle , aspect ratio $S/H = 0.5$ with slanted roofs: \triangle . Black line: Equation (10), grey line: Equation (4), dashed lines: scatter range of RdS profiles shown in (a)).

p41: Figure 10 from Kastner-Klein & Rotach (2004)